Physics of Fluids

Bio-inspired *in silico* microswimmer: Run and tumble kinematics

Cite as: Phys. Fluids **35**, 031908 (2023); https://doi.org/10.1063/5.0142836
Submitted: 17 January 2023 • Accepted: 26 February 2023 • Accepted Manuscript Online: 28 February 2023 • Published Online: 17 March 2023

Wanho Lee (이완호), **Yongsam Kim** (김영삼) **and** **Sookkyung Lim** (임숙경)

Physics of Fluids ARTICLE scitation.org/journal/phf

Bio-inspired *in silico* microswimmer: Run and tumble kinematics

Cite as: Phys. Fluids **35**, 031908 (2023); doi: 10.1063/5.0142836
Submitted: 17 January 2023 · Accepted: 26 February 2023 ·
Published Online: 17 March 2023

View Online Export Citation CrossMark

Wanho Lee (이완호),[1] Yongsam Kim (김영삼),[2] and Sookkyung Lim (임숙경)[3,a)]

AFFILIATIONS

[1]National Institute for Mathematical Sciences, Daejeon 34047, South Korea
[2]Department of Mathematics, Chung-Ang University, Seoul 06974, South Korea
[3]Department of Mathematical Sciences, University of Cincinnati, Cincinnati, Ohio 45221, USA

[a)]Author to whom correspondence should be addressed: sookkyung.lim@uc.edu

ABSTRACT

We present an *in silico* microswimmer motivated by peritrichous bacteria, *E. coli*, which can run and tumble by spinning their flagellar motors counterclockwise (CCW) or clockwise (CW). Runs are the directed movement driven by a flagellar bundle, and tumbles are reorientations of cells caused by some motors' reversals from CCW to CW. In a viscous fluid without obstacles, our simulations reveal that material properties of the hook and the counterrotation of the cell body are important factors for efficient flagellar bundling and that longer hooks in mutant cell models create an instability and disrupt the bundling process, resulting in a limited range of movement. In the presence of a planar wall, we demonstrate that microswimmers can explore environment near surface by making various types of tumble events as they swim close to the surface. In particular, the variation of tumble duration can lead the microswimmer to run in a wide range of direction. However, we find that cells near surface stay close to the surface even after tumbles, which suggests that the tumble motion may not promote cells' escape from the confinement but promote biofilm formation.

I. INTRODUCTION

Artificial microswimmers inspired by natural swimming microorganisms, such as bacteria, have been an interest of many scientists.[1–4] Of the motile microorganisms, bacteria propelled by helical flagella have shown significant potential to be applicable for biomedical devices.[5–9] Flagellated bacteria have a cell body, which typically takes the form of a sphere, a spherocylinder, or a helical shape, and they are generally classified into four groups based on flagellar distribution: monotrichous, a single polar flagellum at one end; lophotrichous, a tuft of flagella at one end; amphitrichous, a single or tuft at both ends; and peritrichous, multiple flagella distributed over the cell body. Variations of such groups are also available; for example, *Magnetococcus marinus* are equipped with two sheathed bundles of flagella on one pole of the spherical cell body.[10] A common characteristic of such bacteria is that they have rotary motors embedded into the cell body that can turn either clockwise (CW) or clockwise (CCW) and drive the flagellar rotation so that flagella can create thrust to move the cell body, which counterrotates to the flagella.

Peritrichous bacteria, such as *E. coli*, explore fluid environment by alternating runs and tumbles in which runs roughly draw straight paths in viscous fluids without environmental obstacles, whereas tumbles lead abrupt changes in the swimming direction.[11–13] During a run, all flagellar motors turn CCW and flagella form a left-handed bundle, which pushes the cell body forward. During a tumble, some of the motors reverse and initiate flagellar unbundling, which turns the cell body into a different swimming direction. In this paper, we investigate the dynamics of an *E. coli* cell model in two aspects: (1) how is flagellar bundling influenced by the hook's material property and the counterrotation of the cell body? and (2) how do cells near a planar wall modify swimming paths using run-and-tumble motion?

Flagellar bundling and unbundling that lead to runs and tumbles, respectively, are important events of bacterial locomotion.[12,13] It is computationally reported that flagellar bundling is affected by flagellar distribution associated with the number and location of flagella and that stiffness of the helical filament must be in a certain range for the flagella to bundle properly.[14] In this work, we focus on the hook known as a universal joint that links the rotary motor to the helical filament. The hook is much more flexible than the filament, and the typical length of the wild type is ∼55 nm.[15–19] The flexibility and the length of the hook may be important factors for flagellar bundling and

even for reorientation. Another factor that we consider is the counter-rotation of the cell body, which has been questioned about its role in bundle formation.[20–23] It is reported that either flagellar hydrodynamics or the cell body rotation alone still makes flagella bundle.[21,23–25] Therefore, we investigate the contribution of the flagellar hydrodynamics and the cell body rotation to the bundling process while incorporating the hook compliance.

Cell motility changes when bacteria get close to a solid surface due to the hydrodynamic interaction between motile microorganisms and the surface. It is experimentally and theoretically reported that cells near surfaces tend to circle,[26–31] in particular, drawing CW circular trajectory when the cell runs with a left-handed flagellar bundle. Bacteria accumulate and spend a long residence time near the surface, and hence, they are likely to be trapped near the surface.[32–37] There have been many studies on flagellated bacteria near surfaces focusing on the run motion. However, little attention has been paid to the tumble motion near surfaces since the first report from three-dimensional tracking by Frymier *et al.*[27] Some studies suggested that tumbles may allow cells to escape from the surface or tumbles may be hindered near a solid surface.[33,38,39] Recently, Lemelle *et al.* investigated tumble kinematics of *E. coli* near a solid surface and identified tumbles as events starting in abrupt deceleration and finishing in abrupt reacceleration of the body motion.[26] In this paper, we investigate the run-and-tumble motion near a solid surface with or without a shear flow, which may be the first study with a full three-dimensional bacteria model immersed in a viscous fluid.

In order to explore the maneuverability of peritrichous bacteria in a free space, we employ the same method previously developed by Lim *et al.*[14] The cell body is modeled as a neutrally buoyant rigid body, the flagella are described by helical elastic rods based on a non-standard Kirchhoff rod theory, and the cell interacts with a viscous fluid using the regularized Stokeslet formulation. The rotary motor generates the torque so that the flagella rotate and the cell body counterrotates under the force- and torque-free conditions. Furthermore, in order to investigate the run-and-tumble motion of multi-flagellated bacteria near surface, we incorporate the image method to account for the effect of a planar wall on the cell motility, which was developed by Park *et al.*[40] for a toy model consisting of a spherical or spheroidal cell body and a single flagellum attached to the cell surface. The image method satisfies zero flow boundary conditions at the infinite planar wall.[40–42]

II. MATHEMATICAL FORMULATION

We use the mathematical model for the bacterial locomotion developed by Lim and her collaborators[14,25,43,44] and summarize it here. Equations of motion consist of three parts: the cell body dynamics, flagellar dynamics, and hydrodynamics of a cell.

First, we model the cell body with the shape of a spherocylinder as an approximately rigid body using a penalty method. The cell surface is discretized by a collection of n_b points, and the reference configuration of the rigid body is denoted by the time-independent vectors $\mathbf{Z}_m$ satisfying the condition $\sum_{m=1}^{n_b} \mathbf{Z}_m = 0$. Then, the configuration of the rigid body at time t, $\mathbf{Y}_m^b(t)$, is given by

$$\mathbf{Y}_m^b(t) = \mathbf{C}(t) + \mathscr{R}(t)\mathbf{Z}_m, \quad m = 1, \ldots, n_b, \tag{2.1}$$

where $\mathbf{C}(t)$ is the centroid of $\{\mathbf{Y}_m^b,\ m = 1, \ldots, n_b\}$ and $\mathscr{R}(t)$ is a rotation matrix.

To enforce the rigidity of the cell body, we use two Lagrangian descriptions of the discretized cell body surface; $\mathbf{X}_m^b(t)$ and $\mathbf{Y}_m^b(t)$, $m = 1, \ldots, n_b$. The former interacts with the surrounding fluid, while the latter has no interaction with the fluid and moves as a rigid body. For each m, the markers $\mathbf{X}_m^b(t)$ and $\mathbf{Y}_m^b(t)$ are coupled by a stiff spring, which generates the following force:

$$\mathbf{F}_m^b(t) = K(\mathbf{X}_m^b(t) - \mathbf{Y}_m^b(t)), \tag{2.2}$$

where K is a penalty parameter that determines how tightly the two Lagrangian markers are tied together. This penalty force acts on $\mathbf{Y}_m^b$, and $-\mathbf{F}_m^b(t)$ becomes a body force on the fluid.

Let $\mathbf{f}^b(t)$ and $\mathbf{n}^b(t)$ be the sum of all external forces and torques, respectively, acting on the body other than those generated from the coupling springs. When $\mathbf{X}_m^b(t)$, $\mathbf{f}^b(t)$, and $\mathbf{n}^b(t)$ are known at any time, the balance equations for the cell body are given as follows:

$$0 = \mathbf{f}^b + \sum_{m=1}^{n_b} \mathbf{F}_m^b(t), \quad 0 = \mathbf{n}^b + \sum_{m=1}^{n_b} (\mathscr{R}(t)\mathbf{Z}_m) \times \mathbf{F}_m^b(t). \tag{2.3}$$

At each time t, we solve Eqs. (2.2) and (2.3) for $\mathbf{C}(t)$ and $\mathscr{R}(t)$ to determine $\mathbf{Y}_m^b(t)$.

Second, to describe the flagellar dynamics, we employ Kirchhoff rod theory since the flagellum is a long but thin filamentous structure. Each flagellum is composed of a rotary motor, a short flexible hook, and a long helical filament. The hook links the filament to the motor, which generates torque and, thus, drives the flagellar rotation, see Fig. 1. For simplicity, we describe equations of motion for a single flagellum. Multiple flagella can be attached to the cell body in the same manner described below. The Kirchhoff rod can be described in the Lagrangian form as $\{\mathbf{X}(s,t), \mathbf{D}^1(s,t), \mathbf{D}^2(s,t), \mathbf{D}^3(s,t)\}$, where $\mathbf{X}(s,t)$ is a three-dimensional space curve and $\{\mathbf{D}^1(s,t), \mathbf{D}^2(s,t), \mathbf{D}^3(s,t)\}$ is its associated orthonormal triad, where s is a Lagrangian

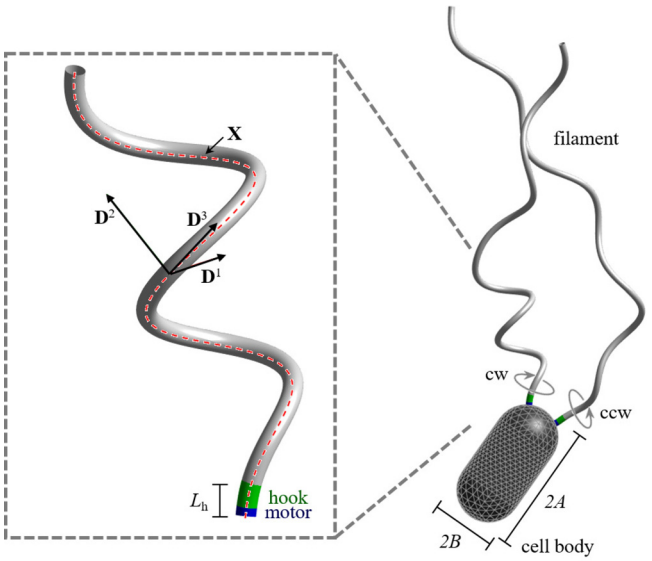

FIG. 1. A schematic diagram of a computational microswimmer with two flagella. Each flagellum consists of a rotary motor embedded in the cell body and a helical filament that is linked to the motor via a short compliant hook.

parameter ranging from $0 \le s \le L$ with $L = L_h + L_f$, and t is the time. Here, L_h and L_f denote the lengths of the hook and the filament, respectively. The reference helical flagellum is defined as[45]

$$\mathbf{X}_0(s) = (r(s)\cos(ks), r(s)\sin(ks), s), \tag{2.4}$$

where k is the wave number. The helical radius $r(s)$ is zero for $0 \le s \le L_h$ and $r(s) = R(1 - e^{-c(s-L_h)^2})$ for $L_h \le s \le L_h + L_f$, where R is the helical radius of the flagellum. We construct the initial configuration of a Kirchhoff flagellum $\mathbf{X}(s,0)$ by attaching $\mathbf{X}_0(s)$ normally to the surface of the cell body and by setting $\mathbf{D}^3(s,0)$, $\mathbf{D}^1(s,0)$, and $\mathbf{D}^2(s,0)$ to be the unit tangent vector, the principal normal, and binormal vectors to $\mathbf{X}(s,0)$, respectively, see Fig. 1. Note that our model flagellum is only approximately inextensible and, hence, s is not arc length, in general. In our computations, the flagellum is reparametrized by arc length before being used and is discretized with equally spaced points along the filament.

To describe forces and torques of a rotating flagellum, we let the internal forces and torques that are transmitted across a section of the flagellum be denoted by $\mathbf{F}$ and $\mathbf{N}$, respectively, and let the applied force and torque densities be denoted by $\mathbf{f}$ and $\mathbf{n}$, respectively. Then, the balance equations for the linear and angular momenta are given as follows:

$$0 = \mathbf{f} + \frac{\partial \mathbf{F}}{\partial s}, \quad 0 = \mathbf{n} + \frac{\partial \mathbf{N}}{\partial s} + \frac{\partial \mathbf{X}}{\partial s} \times \mathbf{F}, \tag{2.5}$$

where

$$\mathbf{F} = \sum_{i=1}^{3} F_i \mathbf{D}^i, \quad \mathbf{N} = \sum_{i=1}^{3} N_i \mathbf{D}^i. \tag{2.6}$$

The constitutive relations are as follows:

$$F_i = b_i \left(\mathbf{D}^i \cdot \frac{\partial \mathbf{X}}{\partial s} - \delta_{3i} \right), \quad i = 1,2,3, \tag{2.7}$$

$$N_i = a_i(s) \left(\frac{\partial \mathbf{D}^j}{\partial s} \cdot \mathbf{D}^k - \Omega_i(s) \right), \quad i = 1,2,3, \tag{2.8}$$

where δ_{3i} is the Kronecker delta and (i, j, k) is any cyclic permutation of $(1, 2, 3)$. $\{\Omega_1, \Omega_2, \Omega_3\}$ describes the intrinsic curvature and twist, which are determined by the helical radius and pitch of the flagellum. Two bending moduli and twist modulus are given as a_1, a_2, and a_3, respectively, and two shearing coefficients and stretching modulus are given as b_1, b_2, and b_3, respectively. The above constitutive relations can be derived from a variational argument of the energy functional given by

$$E = \frac{1}{2} \int \left[\sum_{i=1}^{3} a_i(s) \left(\frac{\partial \mathbf{D}^j}{\partial s} \cdot \mathbf{D}^k - \Omega_i(s) \right)^2 + \sum_{i=1}^{3} b_i \left(\mathbf{D}^i \cdot \frac{\partial \mathbf{X}}{\partial s} - \delta_{3i} \right)^2 \right] ds. \tag{2.9}$$

In order to drive the flagellar rotation, each flagellum is embedded into the cell body normal to the surface at the onset and the motor is located at the bottom of the flagellum. Each motor generates the following constant torque in the normal direction $\mathbf{E}(t)$ at the motor point $\mathbf{X}(s_{\text{mot}}, t)$:

$$\mathbf{N}(s_{\text{mot}}, t) = -\tau \mathbf{E}(t), \tag{2.10}$$

where $|\tau|$ is a parameter that determines the magnitude of the torque, and the motor and, hence, the flagellum rotate counterclockwise when $\tau > 0$ and clockwise when $\tau < 0$. Note that $\mathbf{N}(s_{\text{mot}}, t)$ is the torque of the flagellum onto the motor, which is minus the torque applied by the motor to the flagellum. If a cell has N_f flagella, $\sum_{j=1}^{N_f} \mathbf{N}_j(s_{\text{mot}}, t) = -\sum_{j=1}^{N_f} \tau_j \mathbf{E}_j(t)$ is the total torque applied to the cell body by the N_f motors, which results in counterrotation of the cell body.[14] For simplicity, we use the same value of $|\tau|$ for each flagellum of a cell regardless of the direction of motor rotation.

Finally, we couple the cell to the surrounding fluid governed by the viscous incompressible Stokes equations,

$$0 = -\nabla p + \mu \Delta \mathbf{u} + \mathbf{g}, \quad 0 = \nabla \cdot \mathbf{u}, \tag{2.11}$$

where the fluid velocity $\mathbf{u}$ and the fluid pressure p are unknown functions in terms of the Cartesian coordinates $\mathbf{x}$ and time t, and μ is the fluid viscosity. The regularized force density $\mathbf{g}$ applied to the fluid by the immersed cell is given by

$$\begin{aligned} \mathbf{g}(\mathbf{x}, t) = \sum_{n=1}^{N_f} \Bigg[& \int_0^L (-\mathbf{f}_n(s,t) - \mathbf{f}_n^r(s,t)) \psi_\varepsilon(\mathbf{x} - \mathbf{X}_n(s,t)) ds \\ & + \frac{1}{2} \nabla \times \int_0^L (-\mathbf{n}_n(s,t)) \psi_\varepsilon(\mathbf{x} - \mathbf{X}_n(s,t)) ds \Bigg] \\ & + \sum_{m=1}^{N_b} (-\mathbf{F}_m(t)) \psi_\varepsilon(\mathbf{x} - \mathbf{Y}_m(t)), \end{aligned} \tag{2.12}$$

where N_f is the number of flagella and $\mathbf{f}_n(s,t)$ and $\mathbf{n}_n(s,t)$ are computed using Eqs. (2.5)–(2.8) on the nth flagellum $\mathbf{X}_n(s,t)$. The function $\mathbf{f}_n^r(s,t)$ represents the repulsive force to prevent the contact between the flagella, and the smooth cutoff function ψ_ε, which satisfies $\int_{\mathbb{R}^3} \psi_\varepsilon(\mathbf{r}) d\mathbf{r} = 1$, is defined as

$$\psi_\varepsilon(\mathbf{r}) = \frac{15\varepsilon^4}{8\pi(\|\mathbf{r}\|^2 + \varepsilon^2)^{7/2}},$$

where ε is a regularization parameter.

The motion of each flagellum $\{\mathbf{X}_n, \mathbf{D}_n^1, \mathbf{D}_n^2, \mathbf{D}_n^3\}$ and the marker point $\mathbf{X}_m^b$ that is linked by a stiff spring to the rigid cell body $\mathbf{Y}_m^b$ can be described by

$$\frac{\partial \mathbf{X}_n(s,t)}{\partial t} = \mathbf{u}(\mathbf{X}_n(s,t), t), \tag{2.13}$$

$$\frac{\partial \mathbf{X}_m^b(t)}{\partial t} = \mathbf{u}(\mathbf{X}_m^b(t), t), \tag{2.14}$$

$$\frac{\partial \mathbf{D}_n^i(s,t)}{\partial t} = \mathbf{w}(\mathbf{X}_n(s,t), t) \times \mathbf{D}_n^i(s,t), \quad i = 1,2,3, \tag{2.15}$$

where the angular velocity of the fluid $\mathbf{w}$ is defined as

$$\mathbf{w} = \frac{1}{2} \nabla \times \mathbf{u}(\mathbf{x}, t). \tag{2.16}$$

Computational and physical parameter values used for this work are provided in Table I.

III. RESULTS

Our bio-inspired computational model of a microswimmer allows us to explore swimming properties in a free space filled with fluid or in a confined environment. This paper has three folds: (1) we survey the relationship between applied torque, rotational rates, and

TABLE I. Computational and physical parameters.

Parameters (symbol)	Value
Fluid viscosity (μ)	0.01×10^{-4} g/(μm s)
Mesh width for flagellum (Δs)	0.0304 μm
Number of material points of each rod	300
Number of points of the cell body (N_b)	770
Regularization parameter (ε)	$3\Delta s$
Time step (Δt)	2×10^{-8} s
Cell body length ($2A$)	2 μm (Refs. 11 and 12)
Cell body width ($2B$)	1 μm (Refs. 11 and 12)
Length of filament (L_f)	9.09 μm (Refs. 12, 13, and 46)
Bending modulus of filament ($a_1 = a_2 = a$)	0.0035 g μm^3/ s^2 (Ref. 47)
Twist modulus of filament (a_3)	0.0035 g μm^3/ s^2
Shear modulus ($b_1 = b_2$)	1 g μm/ s^2
Stretch modulus (b_3)	1 g μm/ s^2
Length of hook (L_h)	0.0608 μm (Refs. 15–19)
Bending modulus of hook ($a_1^{hook} = a_2^{hook} = a^{hook} = a/20$)	0.000 175 g μm^3/ s^2
Twist modulus of hook ($a_3^{hook} = a_3$)	0.0035 g μm^3/ s^2

fluid viscosity; (2) we investigate important factors that influence flagellar bundling in a free space; and (3) we investigate run-and-tumble kinematics near wall.

A. Survey on motor torque, rotation rates, and fluid viscosity

In this section, we consider a cell model with a single polar flagellum to investigate rotation rates of the flagellum and the cell body as functions of the applied torque (τ) and fluid viscosity (μ). The flagellum takes the representative form of either a normal left-handed helix with a helical pitch of 2.1611 μm and a radius of 0.2116 μm, or a semicoiled right-handed helix with a helical pitch of 1.0766 μm and a radius of 0.3810 μm. As the rotary motor generates torque, the motor rotation drives the rotation of the flagellum and at the same time the cell body counterrotates under the force- and torque-free conditions. Figure 2 demonstrates that rotation rates of both the flagellum (w_f) and the cell body (w_b) linearly increase as the applied torque increases, while the fluid viscosity is being held fixed. However, when the applied torque is fixed as constant, rotation rates of the flagellum and the cell body are inversely proportional to the fluid viscosity. The relations can be found using the least squares data fitting as

$$\begin{aligned} w_f^{normal} &= 0.8796\tau/\mu, \\ w_f^{semicoiled} &= 0.4604\tau/\mu, \\ w_b &= 0.2144\tau/\mu. \end{aligned} \tag{3.1}$$

When the applied torque and the fluid viscosity are being held fixed, the rotation rate of the normal flagellum is approximately twice faster than that of the semicoiled flagellum and the same goes for the swimming speed. Note that the body rotation rate remains the same independent of the flagellum type as long as the geometry of the cell body is the same. For the rest of work in this paper, we set fluid viscosity to be 0.01×10^{-4} g/(μm s) and the applied torque to be 1.1×10^{-3} (g μm^2/s^2) so that the motor rotation rate and swimming speed are approximately 100 Hz and 10 μm/s, respectively, as observed in wild-type *E. coli* cells.[11,13]

B. Effect of hook's properties on bundling

Compliant hooks that can bend up to 90° from the rotational axis of the motor are known to play an important role in bacterial flagella bundling.[48,49] Together with the flexibility of the hook, the distances between the points at which flagella originate from the cell body may also influence the ability of the flagella to bundle. To investigate this, we place three flagella uniformly on the same latitudinal line of the cell body at which the flagellar axis is normal to the cell body surface. We characterize the flagellar location by its block angle α, which is defined as the angle between the polar axis and the flagellar axis at the onset, see Fig. 3(a). The smaller the angle is, the closer it is to the pole, and therefore, the closer are the bases of the three flagella. To assess the extent to which bundling has occurred, we choose two of the three flagella and measure the limiting distance between their free ends, once the motion has become steady. In these simulations, all flagella are in the normal form and rotate CCW at approximately 100 Hz. Figures 3(b)–3(d) show the limiting distance as functions of the block angle and the bending modulus of the hook when the flagellar length is given as $L_f = 6$, 9, and 12 μm. Large values of the limiting distance, indicated by gray bars, imply that three flagella do not bundle and independently rotate with some steady distance, whereas the values that are close to zero indicate that the flagella form a bundle and rotate closely side by side. Our simulation results demonstrate that both the flexibility of the hook and the proximity of flagellar motors are important factors that control the possibility of flagellar bundling. We can see that stiffened hooks disrupt bundle formation unless their motor points, at which the flagella is attached to the cell body, are close enough, as observed in experiments.[49] We can also observe that the longer the flagellar length L_f is, the more likely the bundle is formed. Note that, whereas bars in gray represent unbundling cases, the rest colors indicate the time when the flagellar bundle starts to form.

C. Role of the cell body in bundling

The role of the cell body in flagellar bundling has been questioned.[20–23] It has been reported that hydrodynamic interaction between flagella can cause bundling even without the counterrotation of the cell body,[21,24,25] but it is also known that rotation of the cell body is sufficient to form a bundle even among passive flagella.[23] To investigate the effect of the cell body on bundling, we consider four different settings depending on the ability of the cell body's rotation and translation: a free swimmer (the cell body can both rotate and translate), a cell with a fixed cell body center (rotate but not translate), a cell with a fixed body frame (translate but not rotate), and a cell with a fixed cell body (neither translate nor rotate). Figure 4 displays the classification for bundling and unbundling for the four settings as the bending modulus of the hook a_{hook} and the block angle α vary. Figures 4(a) and 4(b) demonstrate that the rotation of the cell body and the flexibility of the hook are important in the bundling process.

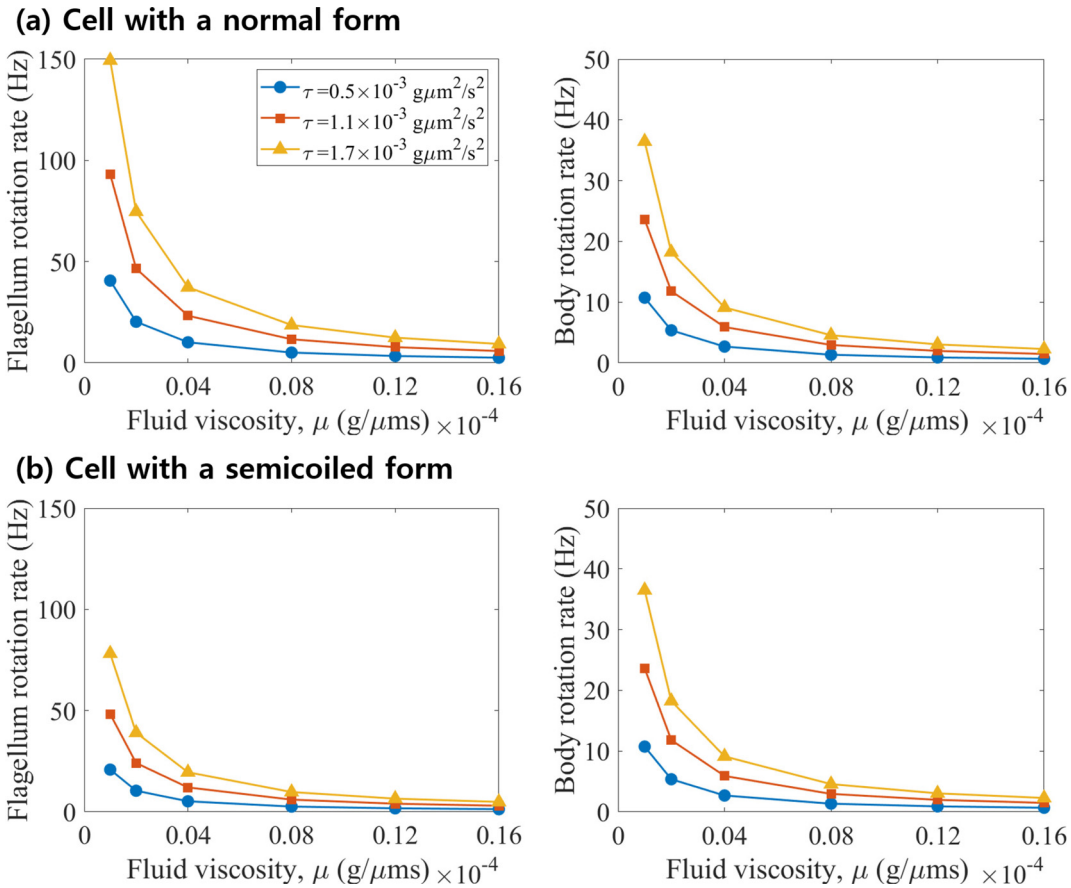

FIG. 2. Rotation rates as functions of the fluid viscosity for various applied torques for a cell with a normal form (a) and a cell with a semicoiled form (b). Rotation rates of the flagellum and the cell body are proportional to the applied torque, but they are inversely proportional to fluid viscosity.

The irrotational cell body predominantly decreases the chance of flagellar bundling, see Figs. 4(c) and 4(d). In the free swimming, the cell body's rotation enhances the flagellar bundling and enlarges the scope of flagellar distance and the hook compliance for the flagellar bundling to occur.

D. Run-and-tumble in a free space

Peritrichous bacteria, such as *E. coli*, alternate two modes of motility: runs and tumbles. Runs are approximately straight movement with a normal left-handed flagellar bundle rotating CCW, and tumbles are erratic displacement upon motor reversals of some flagella. During a tumble, the associated flagella undergo a sequence of polymorphic transformations from *normal* to *semicoiled* to *curly 1* and then back to the normal state when its motor returns to CCW rotation.[12,13] It is experimentally and computationally reported that normal and semicoiled forms are key polymorphic forms in reorientation.[13,14,50] Hence, we omit curly 1 form in all simulations below.

In this section, the model cell has three flagella, which are equally spaced on a latitudinal line near the pole, one of which undergoes polymorphic transformations from normal to semicoiled and back to normal polymorphism as the associated motor reverses from CCW to CW and then back to CCW. Cells run and tumble repeatedly in a free space, while run and tumble durations are fixed as 0.3 and 0.1 s, respectively. Figure 5(a) (Multimedia view) shows an exemplary trajectory of the centroid of the cell body in the case of block angle $\alpha = 30°$. The inset of Fig. 5(a) illustrates the configurations of the cell at some selected times together with a trajectory of the cell body center for the time duration of 0.5 s during which the cell undergoes a run and a tumble, and then a new run, which corresponds to the thick line of the whole trajectory. When the designated flagellum experiences a polymorphic transformation from normal to semicoiled states upon the motor reversal from CCW to CW, the flagellum leaves the bundle and turns the cell body, resulting in the change in the swimming direction for the next run. Another motor reversal from CW to CCW leads the designated flagellum to transform back into the normal form and to rejoin the bundle tightly.[12,13,24] Note that the trajectory has shown a similar pattern during each of the repeated run-and-tumble, since the durations of runs and tumbles are fixed. Variations of these durations may change the swimming trajectories.

In order to measure the reorientation caused by a tumble, we define a tumble angle θ as the angle between two consecutive straight runs. Figure 5(b) shows the mean and the standard deviation of tumble angles of the repeated run-and-tumble for various values of the block angle, $\alpha = 10°$, $20°$, $30°$, $40°$, $50°$, and $60°$. In general, as the

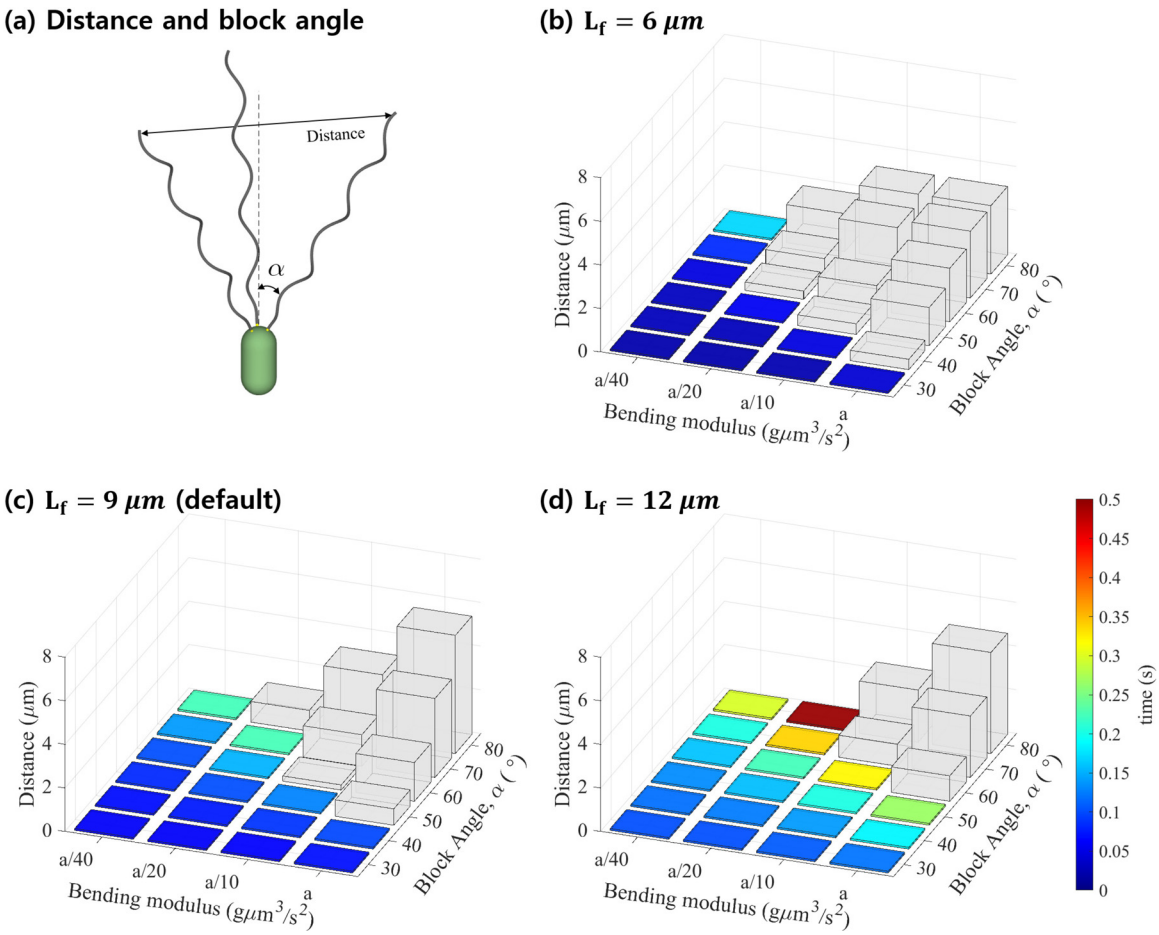

FIG. 3. Bundle formation can be affected by the bending modulus of the hook (a_{hook}), flagellar length (L_f), and block angle (α), where α is defined as the angle between the cell body axis and the flagellar axis at the onset (a), and L_f is set as 6 (b), 9 (c), and 12 μm (d). After the cell reaches a steady run motion in a sense that bacteria run straight at a constant swimming speed and the distance between flagella remains constant, limiting distance between the tips of the flagella indicates the success of flagellar bundling with small values in colors and the failure of bundling (unbundling) with large values in gray. The colorbar represents the time when the flagellar bundle starts to form.

block angle gets larger, the average tumble angle increases following a trend of a step function. When the block angle is very small and hence flagella stay close to each other, the average tumble angle is also small, which implies that the swimming directions of the old and new runs are almost aligned with each other. As the block angle increases, the tumble angle increases dramatically and stay around 30° for the range of $30° < \alpha < 50°$. There is another jump when α is further increased to 60°.

E. Effect of hook lengths on runs and tumbles

Recently, Erhardt *et al.*[19] revealed that the length of the hook is controlled in a sophisticated manner on a nanometer scale and that the motility performance is optimal around the wild-type (WT) hook length. To investigate the effect of hook length on bacterial swimming, we consider cells with four identical flagella, in which the hook lengths of all four flagella are set to be one of the following four different values: 0, 60 (WT), 120, or 180 nm. Then, one of the four flagella goes through a series of polymorphic transformations as in Sec. III D.

Our simulations demonstrate that the length of the hook influences flagellar propulsion. The cell with no hook swims faster during runs but fails in bundle formation, since all the flagellar parts near the motors are less compliant and resist bending, and thus, the four flagella independently work, even though they are placed near one pole of the cell body. Moreover, the tumble angle is substantially increased in comparison with that of the wild type cell as shown in Table II. In the presence of hooks, the flagellar bundle is formed earlier and tightened more firmly as the hook gets longer. However, the flagella with longer hooks create a buckling instability when the cell swims, which interrupts reorientation of the cell during a tumble and causes the cell body to wobble during a next run. Figure 6 (Multimedia view) shows time evolution of the cell movement and its trajectory when the hook length L_f is 60 (top) and 180 nm (bottom). During the first run ($t = 0.4$ s), the axes of the cell body in both cases are well aligned with the flagellar axes because their initial configurations are approximately symmetric about the body axis. During a tumble ($t = 0.5$ s), the transforming flagellum leaves the bundle in the wild type cell; however, the

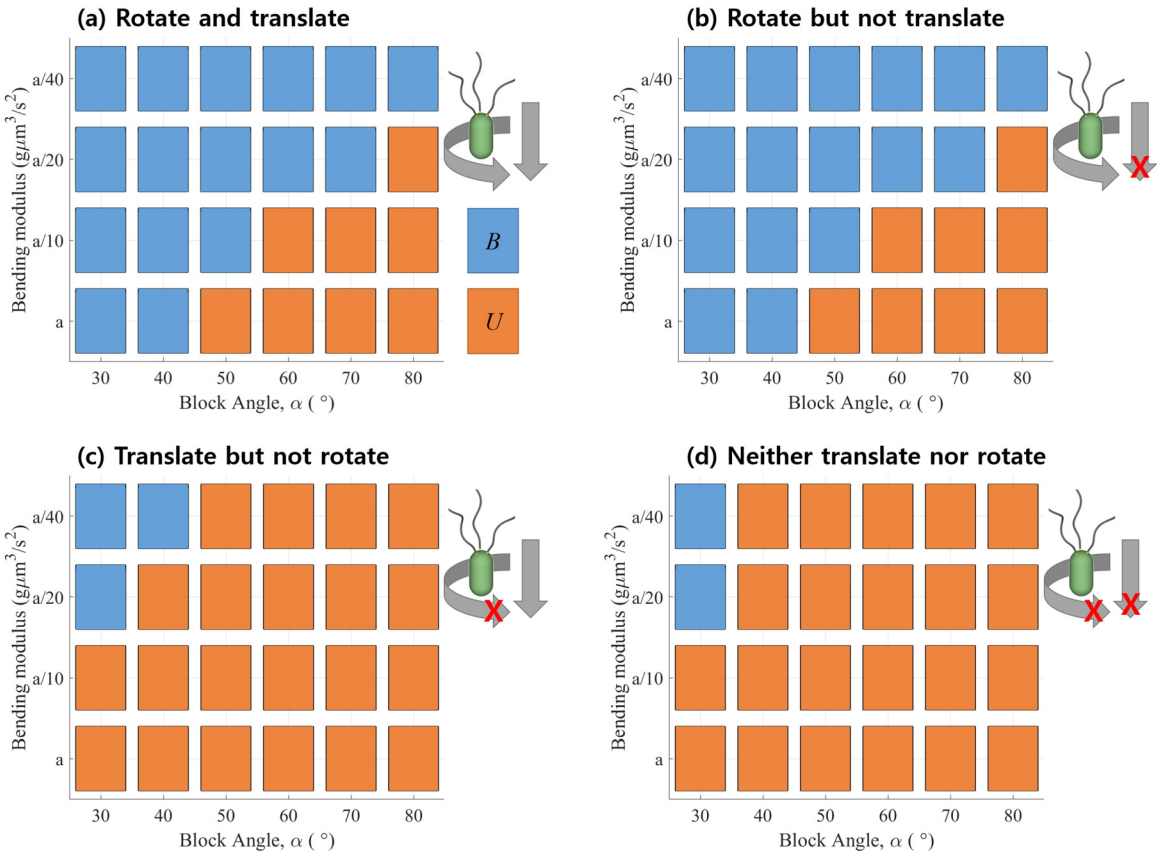

FIG. 4. Classification of flagellar bundling (blue) and unbundling (orange) for various bending moduli of the hook a_{hook} and various block angle α in the four different settings of the cell body that can rotate and translate (a), rotate but not translate (b), translate but not rotate (c), and neither translate nor rotate (d).

transforming flagellum still stays close to the bundle in the mutant cell with the longer hooks, which induces the small tumble angle and the wobble dynamics of the cell body. Note that during the second run ($t = 0.6$–0.7 s), the cell with normal hooks maintains the body axis and the bundle axis in the same direction, whereas the cell with longer hooks leads the cell body axis to deviate from the flagellar bundle axis at a certain angle, which makes the cell body to wobble periodically as the cell runs.

F. Surface exploration through run-and-tumble motion

Peritrichous bacteria explore in a free space by alternate runs and tumbles. Such bacteria frequently encounter complex environments, such as physical barriers and flow shear, and, hence, the run-and-tumble motion is likely to be altered as opposed to that in a free space. In this section, we consider a cell with a left-handed flagellar bundle formed by three flagella and place it near a planar wall in the absence/presence of the shear flow in the background and investigate swimming behavior of bacteria, which is determined by hydrodynamic interaction of the cell with the surrounding environmental conditions.

In the presence of the planar wall, the hydrodynamic torque due to the wall changes the straight run path in the free space into a persistent CW circular path with almost constant height from the wall, see the swimming motion of a single cell in Fig. 7(a) (Multimedia view). Three trajectories are drawn by following the center of the cell body (blue), one point on the cylindrical cell surface (green) and the tip of one flagellum (brown), each of which shows periodic oscillatory behavior with small amplitude while drawing a large circular path in the CW direction. Enlargement of the trajectories around $t = 4.875$ s is put in the inset in the middle.

Tumble events cause bacteria to deviate from the smooth circular path and lead into the new direction. Figure 7(b) illustrates some representative trajectories of the centroid of cells in which the circular runs are interrupted by three different types of tumble conditions. The very first run denoted by B (black line) is interrupted by the first group of tumble events, which is classified by which and how many flagella transform, denoted by $F_{i,j,k}$, where i, j, and k indicate the index of the transforming flagellum (blue lines). The second run in the case of $F_{1,2,3}$ meets the second group of tumble events, which is classified by different tumble durations, denoted by $D_\ell = (0.1 + 0.02\ell)$ s (red lines). The third run in the case of D_0 is interrupted by the last group of tumble events, which is classified by the initiation time of tumble,

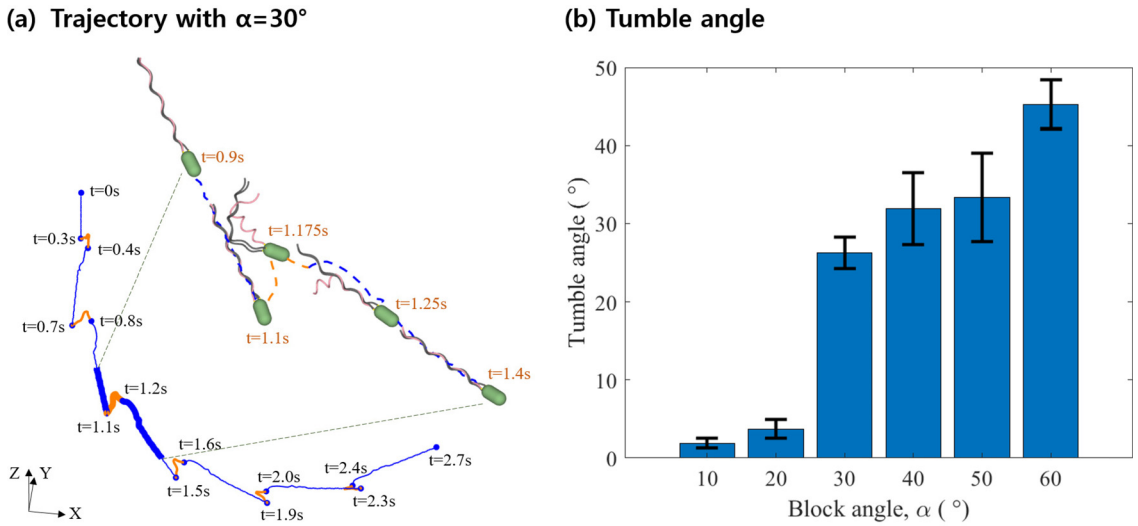

FIG. 5. Repeated run-and-tumble motion and the resultant tumble angles of cells in a free space. Each cell has three flagella and experiences repeatedly over time the following process: one of the flagella goes through a series of polymorphic transformations from normal to semicoiled and then back to normal as the associated motor reverses from CCW to CW and then to CCW. Left panel shows a sample trajectory of the centroid of the cell body that alternates runs (blue) and tumbles (orange) when the initial block angle is given as $\alpha = 30^{\circ}$. Run and tumble durations are fixed at 0.3 and 0.1 s, respectively. The inset illustrates snapshots in the process of a run and a tumble followed by another run, which corresponds to the time interval from $t = 0.9$ s to $t = 1.4$ s. Right panel shows the mean and the standard deviation of tumble angles between any two consecutive runs as the block angle α varies. Multimedia view: https://doi.org/10.1063/5.0142836.1

denoted by $T_\ell = 0.005\ell$ s, in which motor reversals are initiated at different times over two cycles of the flagellar rotation (purple curves). All three flagella go through polymorphic transformations at the same time during tumbles in the second and the last groups of tumbles.

We can see that, during the new run after a tumble, trajectories eventually go back to a CW circular path except for the case of the indefinite tumble duration D_∞ in which all the flagella are of the right-handed semicoiled form turning CW and the cell draws a smooth CCW trajectory. We can also see that the reoriented directions due to the tumbles are different depending on the different cases in each group of tumbles. Note, however, that the representative trajectories in Fig. 7(b) for the first and last groups include the maximum range of reoriented directions within each group. This illustrates that the direction of reorientation is limited as opposed to the cells in a free space. For example, it is computationally reported that cells in a free space can be reoriented sweeping out 0 to 2π in longitude and 0 to $\pi/2$ in turning angle by running through all the phases of the initiation time of tumble over a single cycle of the cell body rotation.[14] Unlike the cells in the first and last groups, the cells in the second group follow a circular CCW path of D_∞ during the tumble duration and then switch to a CW path in the new run, demonstrating that the tumble duration can lead the cell to be reoriented in a wide range of the direction. It is interesting to see that the cells remain close to the wall before and after tumbles in any group, i.e., they are trapped near wall, which suggests that tumbles may not be an efficient strategy for a cell to escape from the wall. This implies that the hydrodynamic interaction of cells with surfaces may always promote the opportunity for the cell to be adhered to the surfaces so that they can form biofilm.[37] Recently, Junot *et al.*[51] found long surface residence times and frequent tumbling during the residence near surface before escaping, confirming that tumbling would be an inefficient escape mechanism. However, they also reported that escape is tightly coupled to tumble and most cell escapes from the surface indeed occur immediately after a tumble. A further study is needed to find conditions that make the cell escape.

TABLE II. Measurements of reorientations with various hook lengths.

Hook length (nm)	no hook	60 (WT)	120	180
Tumble angle, θ (°)	46.55	14.91	3.89	3.65

Lemelle *et al.*[26] reported that run-and-tumble motion near a planar wall is different from that in a free space and that tumbles near a wall appear to take a longer time, following deceleration–reorientation–acceleration pattern. Our simulations also show a similar trend to those observed in experiments, see the representative case in Fig. 8(a), which shows time evolution of the time-averaged swimming speed of the case D_{10} during the run-and-tumble motion near a solid surface. The swimming speed in Fig. 8(a) displays the three phases: deceleration–reorientation–acceleration, which is the common feature of tumble events near a solid wall. There is a drop in swimming speed in the beginning of the tumble, and the cell maintains a low speed during reorientation and then accelerates during the transition toward the new run. Two shaded areas indicate the time period of transitions from normal (CCW) to semicoiled (CW) and vice versa. The pattern of average speed is consistent with other trajectories in the second group except for the case of D_3, which has a tumble duration of 0.16 s. This demonstrates that there is a threshold of tumble duration to maintain this pattern, see Fig. 8(b), which displays time evolutions of the swimming speed of all cases in the second group. Note that the phase duration of reorientation is linearly proportional to the tumble duration. Time evolutions of the swimming

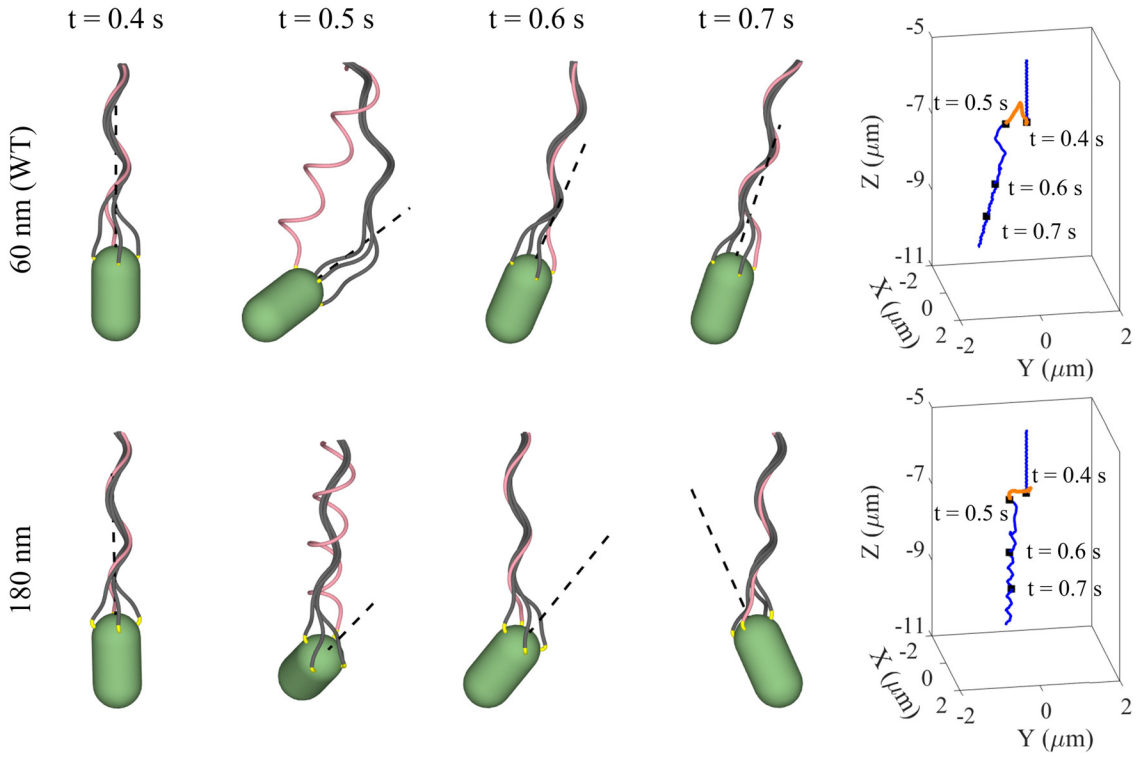

FIG. 6. Comparison of close-up snapshots near hooks and the trajectories of cells with two different hook lengths. The cell has four identical flagella, and the length of hooks is given as 60 nm (top, wild-type) or 180 nm (bottom). One flagellum in pink undergoes polymorphic transformations. Dashed lines indicate the cell body axes. Boxes on the right show trajectories of the centroid of each cell body. The trajectory in blue and orange colors corresponds to runs and tumbles, respectively. Multimedia view: https://doi.org/10.1063/5.0142836.2

speed in other groups show the pattern similar to that of D_3 because the tumble duration in those cases is given as 0.1 s, which is slightly shorter than the case of D_3.

We now investigate the hydrodynamic interaction between bacteria and the perturbed ambient flow in the presence of a planar wall. The background flow is a time-independent shear flow, which can be applied by imposing on the whole domain the following velocity field:

$$\mathbf{u}_{\text{shear}}(\mathbf{x}) = \beta(z, 0, 0), \tag{3.2}$$

where z is the z-coordinate of the point $\mathbf{x}$ and β is a constant representing the shear rate. This positive x-directional flow velocity and the associated angular velocity, $\mathbf{u}_{\text{shear}}(\mathbf{x})$ and $\mathbf{w}_{\text{shear}}(\mathbf{x}) = \frac{1}{2}\nabla \times \mathbf{u}_{\text{shear}} = (0, \beta/2, 0)$, respectively, are added to the velocities of the immersed boundaries given in Eqs. (2.13), (2.14), and (2.16).

When the cell is placed near a wall and under the shear flow, the competition between the shear stress from the fluid and the flagellar propulsive force leads to two types of paths depending on the shear rate: periodic skewed coil paths and linear paths, see Fig. 9(a) (Multimedia view). Both types of trajectories oscillate with very small amplitudes but roughly lie on a plane-parallel to the wall, $z = 0$, that is, the height of the cell from the wall remains almost constant. For small values of β, the flagellar propulsion against the shear flow is strong and, hence, creates skewed coiled trajectories in the leftward direction when viewed toward the downstream direction. The wavelength of the helical trajectories gets larger as the shear rate increases. For large values of β, however, the fluid shear stress overcomes the bacterial propulsive force and induces the leftward linear path.

Figure 9(b) shows perturbed trajectories of the case $\beta = 10/\text{s}$ after tumbles caused by transforming different flagella, as done previously. Each tumble is initiated at $t = 15.6$ s with the duration of 0.1 s. The blue curve denoted by B is the trajectory without any tumble. Figure 9(c) shows the corresponding height of the trajectories in Fig. 9(b) from the surface. As shown in figure, tumbles under the shear flow change the swimming direction but the cells after tumbles still stay near the surface and draw skewed coil paths.

IV. SUMMARY AND DISCUSSION

Motivated by peritrichous bacteria, such as *E. coli* cell, we present an *in silico* model of a swimming cell with multiple flagella to understand run-and-tumble motion in a viscous fluid. Flagella are embedded uniformly near one pole of the cell body, and this cell runs by a spinning flagellar bundle and tumbles by some motor reversals. Our simulations show that flagellar bundling is enhanced by the hook flexibility, provided that the flexibility of the hook is in the right range. If the hook is too stiff, it limits the range of flagellar distance for bundling. If it is too flexible, the buckling instability occurs. Similarly, our model shows that optimized hook length is necessary for the formation and proper function of a flagellar bundle. Flagella with hooks that

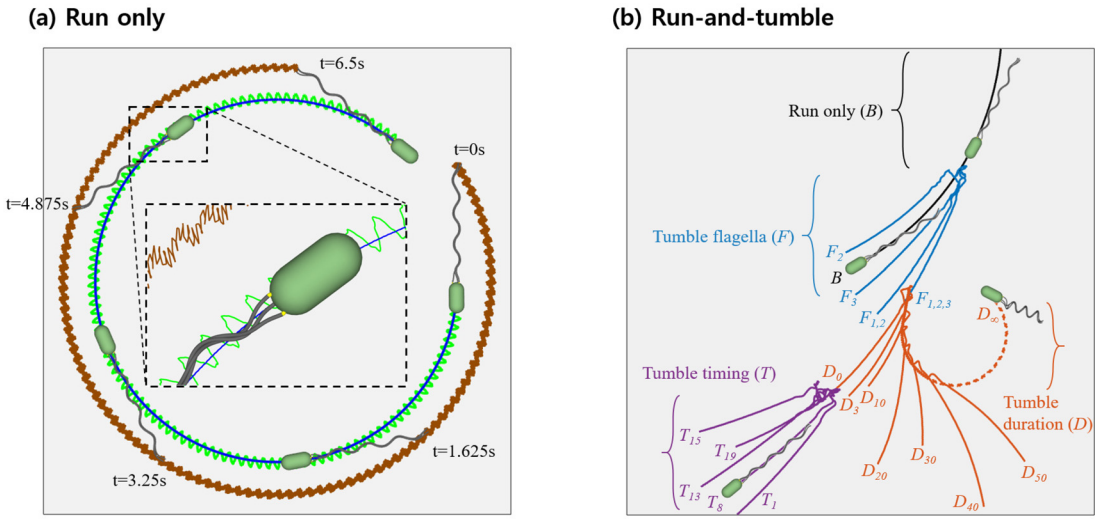

FIG. 7. Trajectories of the run and tumble motion of cells with three flagella located near a planar wall. The left panel shows three circular CW trajectories of a single cell with a persistent run, in which trajectories are drawn by following the center of the cell body (blue), one point on the cylindrical cell body surface (green), and the tip of one flagellum (brown). Enlargement of the trajectories around $t = 4.875$ s is put in the inset in the middle. A tumble event deviates the smooth circular trajectories and leads to different circular paths. The right panel shows representative trajectories caused by different types of tumble conditions. The size of bacteria is scaled up by a factor of two for a better visualization. After a run for a certain period, denoted by B (black curve), the first group of tumble events occurs due to which and how many flagella transform (blue curves), denoted by $F_{i,j,k}$, where i, j, and k indicate the transforming flagella. In the case of $F_{1,2,3}$, the second group of tumble events occurs due to different lengths of tumble duration (red curves), denoted by $D_\ell = (0.1 + 0.02\ell)$ s. Following the case of D_0, the last group of tumble events occurs due to tumble timing (purple curves), denoted by $T_\ell = 0.005\ell$ s, in which motor reversals are initiated at different times over two cycles of the flagellar rotation. All three flagella go through polymorphic transformations at the same time during tumbles in the second and the last groups of tumbles. In the new run after a tumble, trajectories eventually go back to a CW circular path except for the case of the indefinite tumble duration D_∞ in which all the flagella are of the right-handed semicoiled form turning CW and the cell draws a smooth CCW path. Multimedia view: https://doi.org/10.1063/5.0142836.3

are too short are unable to form a bundle, and those with hooks that are too long form bundles that buckle when the cell tries to reorient by reversing some flagella to initiate a tumble. These effects of hook length are similar to those of hook flexibility. This underscores the importance of the control of hook length as reported in Ref. 19.

Cell swimming is constrained by the torque-free condition, and hence, the cell body necessarily rotates in the opposite direction from that of the flagella, which eventually helps the process of flagellar bundling. To demonstrate this, we have artificially prevented rotation and/or translation of the cell body in some of our simulations and have

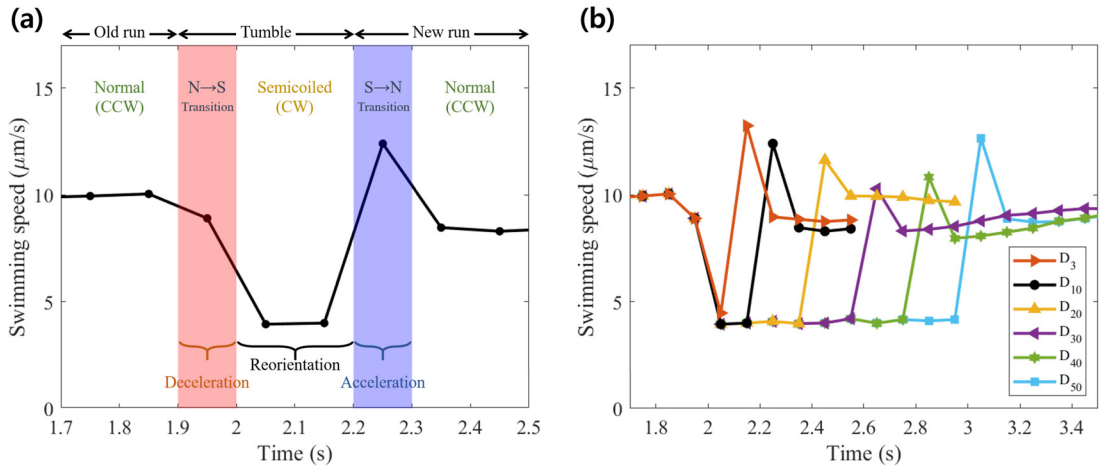

FIG. 8. Time-averaged swimming speed of the cases in the second group during the run-and-tumble motion near a solid surface. (a) A representative case of D_{10} in which the total tumble duration is 0.3 s. The cell displays three phases during a tumble; deceleration (speed drop)–reorientation (low speed)–acceleration (transition). Colored areas indicate the time period of transitions from normal to semicoiled and vice versa. (b) All cases in the second group and demonstrates that there is a threshold of tumble duration that separates D_3 from rest of the cases.

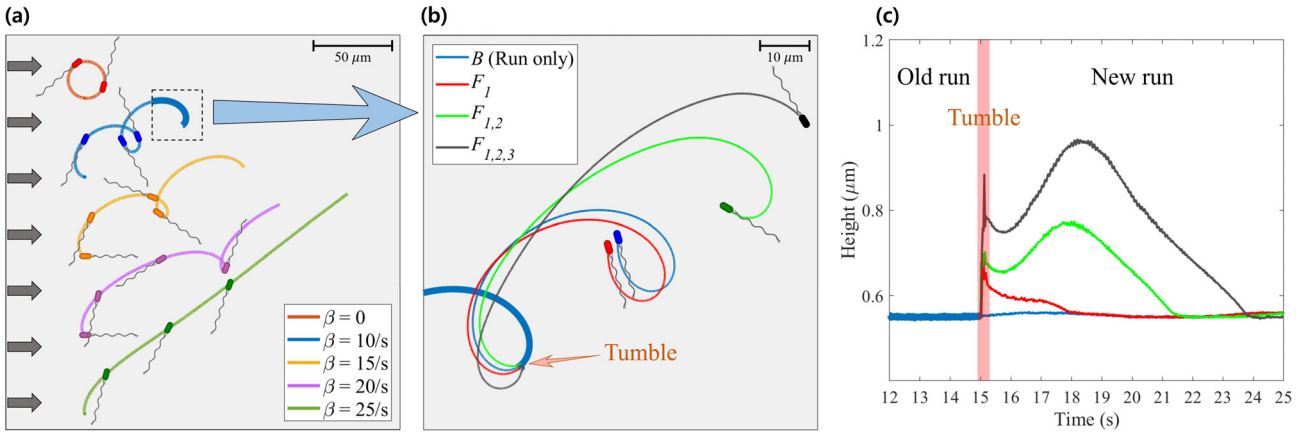

FIG. 9. Cell trajectories under the shear flow in the presence of the planar wall. The left panel shows trajectories of the cell body center when the shear rate β is given at 0, 10/s, 15/s, 20/s, and 25/s. The arrows indicate the direction of the background flow. For each trajectory, configurations of cells are captured at $t = 0$, 3, 6, and 9 s. The middle panel shows perturbed trajectories of the case $\beta = 10/$ s after tumbles caused by transforming different flagella in which each tumble is initiated at $t = 15$ s with the duration of 0.1 s. The blue curve denoted by B is the trajectory without any tumble. For better visualization, the size of bacteria is scaled up by a factor of 4 and 1.5 for (a) and (b), respectively. The right panel shows the corresponding height of the cell trajectories from the surface given in Fig. 9(b). Multimedia view: https://doi.org/10.1063/5.0142836.4

shown that the range of parameters with which bundling occurs is, thereby, narrowed. The extent of counterrotation in our model cell may be exaggerated, however, by our assumption that the flagellar motors are clustered near one pole. If the flagellar motors were more uniformly distributed over the cell body, one would expect the (vectorial) torques produced by those motors on the cell body to cancel.

It is known that bacteria *E. coli* seek to adhere to the surface and form a bacterial colony embedded in a matrix of extracellular polymeric substances (EPS), which protects the microbes from unfavorable environmental conditions, which could result in bacterial infection.[36,52,53] In order to investigate the surface exploration of the cell, different types of tumble events, such as various initiation times and durations of tumbles, are applied in the model. Our simulations demonstrate that as the cell explores the surface through run-and-tumble motion, the hydrodynamic effect of the wall keeps the cell motility near the surface, which suggests that the biofilm formation on the surface may be promoted regardless of cell's ability to tumble and that the tumble dynamics near wall is not for cells' escape from the surface. In contrast to *E. coli*, bacteria *P. putida*, which has a polar flagellar bundle, take the benefit of the wrapping mode when they are often found in physically confined environments.[54–57] The wrapping mode occurs when the polar bundle coils around the cell body and is responsible for reorientation in a free space. Moreover, both experimental and computational data suggest that these cells make use of the wrapping mode to run away from the confinement unlike tumbles in *E. coli*.

In the presence of a solid surface and shear flow, the interplay of hydrodynamic forces on bacteria significantly modifies motility of bacteria. For low shear rates, the flagellar propulsive force dominates against the shear force and, thus, the cell draws skewed helical-like trajectories. For high shear rates, the shear force dominates and leads the cell to linear paths. It is worth mentioning that cells stay close to the surface regardless of various shear rates. Moreover, tumbles under shear flow deviate the running path but still keep the cell near the surface. Our simulations propose that surface tumbles may not promote cell escape from the surface, which may facilitate biofilm formation. However, the shear flow leads cells to the overall downstream motility and, thus, biofilm is less likely to form over a substrate with shear flow.

Our model is idealized and allows us to explore the dynamics of microswimmers. This work may provide insight into the design of an artificial microrobot with potentials to optimize its performance and to control maneuverability as intended. Characteristic features for tumble angles and trajectories determined by material and geometrical properties of bacteria in a free space or in the presence of the physical barriers may be incorporated into the design of micromachines. One of the main interest in this research field is to understand the swimming mechanism of bacteria in complex fluids often found in nature and biology. In particular, it is reported that *E. coli* in non-Newtonian shear flow causes upstreaming motility (i.e., positive rheotaxis) near a surface,[58–60] which can affect bacterial transport in biomedical setting, such as the urinary tract and catheters. Understanding nonlinear rheological behavior in bacterial swimming in complex fluids may help to understand bacterial pathogenesis, which will be the subject of future investigations.

ACKNOWLEDGMENTS

S.L. was supported by NSF (No. DMS-1853591) and the Charles Phelps Taft Research Center at University of Cincinnati, USA. W.L. was supported by the National Institute for Mathematical Sciences Grant funded by the Korean government (No. B23910000). Y.K. was supported by the National Research Foundation of Korea Grant funded by the Korean government (No. 2020R1F1A1A01074981). Many of the computations were performed using computing facilities at the National Institute for Mathematical Sciences (Nos. NFEC-2016-10-212540, 2020H140002, and 2021H110002).

AUTHOR DECLARATIONS

Conflict of Interest

The authors have no conflicts to disclose.

Author Contributions

Wanho Lee: Data curation (lead); Formal analysis (lead); Validation (lead); Visualization (lead); Writing – review & editing (supporting). **Yongsam Kim:** Formal analysis (equal); Investigation (lead); Validation (equal); Writing – review & editing (supporting). **Sookkyung Lim:** Conceptualization (lead); Methodology (lead); Supervision (lead); Writing – original draft (lead); Writing – review & editing (lead).

DATA AVAILABILITY

The data that support the findings of this study are available from the corresponding author upon reasonable request.

REFERENCES

[1]A. Bunea and R. Taboryski, "Recent advances in microswimmers for biomedical applications," Micromachines **11**(12), 1048 (2020).
[2]A. C. H. Tsang, E. Demir, Y. Ding, and O. S. Pak, "Roads to smart artificial microswimmers," Adv. Intell. Syst. **2**, 1900137 (2020).
[3]H.-W. Huang, F. E. Uslu, P. Katsamba, E. Lauga, M. S. Sakar, and B. J. Nelson, "Adaptive locomotion of artificial microswimmers," Sci. Adv. **5**, eaau1532 (2019).
[4]S. Muiños-Lamdin, A. Fischer, V. Holubec, and F. Cichos, "Reinforcement learning with artificial microswimmers," Sci. Rob. **6**(52), eabd9285 (2021).
[5]L. Zhang, J. J. Abbott, L. Dong, B. E. Kratochvil, D. Bell, and B. J. Nelson, "Artificial bacterial flagella: Fabrication and magnetic control," Appl. Phys. Lett. **94**, 064107 (2009).
[6]T. Yanga, B. Sprinkleb, Y. Guoa, J. Qianc, D. Huac, A. Donevb, D. W. M. Marra, and N. Wu, "Reconfigurable microbots folded from simple colloidal chains," Proc. Natl. Acad. Sci. **117**(31), 18186–18193 (2020).
[7]B. Ahmad, M. Gauthier, G. J. Laurent, and A. Bolopion, "Mobile microrobots for In vitro biomedical applications: A survey," IEEE Trans. Rob. **38**(1), 646 (2022).
[8]Y. Alapan, O. Yasa, B. Yigit, I. C. Yasa, P. Erkoc, and M. Sitti, "Microrobotics and microorganisms: Biohybrid autonomous cellular robots," Annu. Rev. Control Rob. Auton. Syst. **2**, 205–230 (2019).
[9]Y. Dong, L. Wang, V. Iacovacci, X. Wang, L. Zhang, and B. J. Nelson, "Magnetic helical micro-/nanomachines: Recent progress and perspective," Matter **5**(1), 77–109 (2022).
[10]K. Bente, S. Mohammadinejad, M. A. Charsooghi, F. Bachmann, A. Codutti, C. T. Lefèvre, S. Klumpp, and D. Faivre, "High-speed motility originates from cooperatively pushing and pulling flagella bundles in bilophotrichous bacteria," eLife **9**, e47551 (2020).
[11]H. C. Berg, "The rotary motor of bacterial flagella," Annu. Rev. Biochem. **72**, 19–54 (2003).
[12]N. C. Darnton, L. Turner, S. Rojevsky, and H. C. Berg, "On torque and tumbling in swimming *Escherichia coli*," J. Bacteriol. **189**, 1756–1764 (2007).
[13]L. Turner, W. S. Ryu, and H. C. Berg, "Real-time imaging of fluorescent flagellar filaments," J. Bacteriol. **182**, 2793–2801 (2000).
[14]W. Lee, Y. Kim, C. S. Peskin, and S. Lim, "A novel computational approach to simulate microswimmers propelled by bacterial flagella," Phys. Fluids **33**, 111903 (2021).
[15]M. Erhardt, T. Hirano, Y. Su, K. Paul, D. H. Wee, S. Mizuno, S. Aizawa, and K. T. Hughes, "The role of the FliK molecular ruler in hooklength control in *Salmonella enterica*," Mol. Microbiol. **75**(5), 1272–1284 (2010).
[16]M. Erhardt, H. M. Singer, D. H. Wee, J. P. Keener, and K. T. Hughes, "An infrequent molecular ruler controls flagellar hook length in *Salmonella enterica*," EMBO J. **30**(14), 2948–2961 (2011).
[17]S. Shibata, N. Takahashi, F. F. Chevance, J. E. Karlinsey, K. T. Hughes, and S. Aizawa, "FliK regulates flagellar hook length as an internal ruler," Mol. Microbiol. **64**(5), 1404–1415 (2007).
[18]T. Hirano, S. Yamaguchi, K. Oosawa, and S. Aizawa, "Roles of FliK and FlhB in determination of flagellar hook length in Salmonella typhimurium," J. Bacteriol. **176**, 5439–5449 (1994).
[19]M. Erhardt *et al.*, "Hook length of the bacterial flagellum is optimized for maximal stability of the flagellar bundle," PLoS Biol. **16**, e2006989 (2018).
[20]R. A. Anderson, "Formation of the bacterial flagellar bundle," in *Swimming and Flying in Nature*, edited by T. Y.-T. Wu, C. J. Brokaw, and C. Brenner (Plenum Press, 1975), Vol. 1, pp. 42–55.
[21]M. Kim, J. C. Bird, A. J. Van Parys, K. S. Breuer, and T. R. Powers, "A macroscopic scale model of bacterial flagellar bundling," Proc. Natl. Acad. Sci. **100**, 15481–15485 (2003).
[22]R. M. Macnab, "Bacterial flagella rotating in bundles: A study in helical geometry," Proc. Natl. Acad. Sci. **74**, 221–225 (1977).
[23]T. R. Powers, "Role of body rotation in bacterial flagellar bundling," Phys. Rev. E **65**, 040903 (2002).
[24]W. Lee, Y. Kim, B. E. Griffith, and S. Lim, "Bacterial flagellar bundling and unbundling via polymorphic transformations," Phys. Rev. E **98**, 052405 (2018).
[25]S. Lim and C. S. Peskin, "Fluid-mechanical interaction of flexible bacterial flagella by the immersed boundary method," Phys. Rev. E **85**, 036307 (2012).
[26]L. Lemelle, T. Cajgfinger, C. C. Nguyen, A. Dominjon, C. Place, E. Chatre, R. Barbier, J. Palierne, and C. Valliant, "Tumble kinematics of *Escherichia coli* near a solid surface," Biophys. J. **118**, 2400–2410 (2020).
[27]P. D. Frymier, R. M. Ford, and P. T. Cummings, "Three-dimensional tracking of motile bacteria near a solid planar surface," Proc. Natl. Acad. Sci. U. S. A. **92**, 6195–6199 (1995).
[28]L. Lemelle, J.-F. Palierne, and C. Place, "Curvature reversal of the circular motion of swimming bacteria probes for slip at solid/liquid interfaces," Soft Matter **9**, 9759–9762 (2013).
[29]E. Lauga, W. R. DiLuzio, G. M. Whitesides, and H. A. Stone, "Swimming in circles: Motion of bacteria near solid boundaries," Biophys. J. **90**, 400–412 (2006).
[30]H. Shum, E. A. Gaffney, and D. J. Smith, "Modelling bacterial behaviour close to a no-slip plane boundary: The influence of bacterial geometry," Proc. R. Soc. A **466**, 1725–1748 (2010).
[31]D. Kim, Y. Kim, and S. Lim, "Effects of swimming environment on bacterial motility," Phys. Fluids **34**, 031907 (2022).
[32]S. Bianchi, F. Saglimbeni, and R. D. Leonardo, "Holographic imaging reveals the mechanism of wall entrapment in swimming bacteria," Phys. Rev. X **7**, 011010 (2017).
[33]M. Molaei, M. Barry, R. Stocker, and J. Sheng, "Failed escape: Solid surfaces prevent tumbling of *Escherichia coli*," Phys. Rev. Lett. **113**, 068103 (2014).
[34]K. Drescher, J. Dunkel, and R. E. Goldstein, "Fluid dynamics and noise in bacterial cell-cell and cell-surface scattering," Proc. Natl. Acad. Sci. U. S. A. **108**, 10940–10945 (2011).
[35]M. A. S. Vigeant and R. M. Ford, "Interactions between motile Escherichia coli and glass in media with various ionic strengths, as observed with a three-dimensional-tracking microscope," Appl. Environ. Microb. **63**, 3474–3479 (1997).
[36]A. P. Berke, L. Turner, H. C. Berg, and E. Lauga, "Hydrodynamic attraction of swimming microorganisms by surfaces," Phys. Rev. Lett. **101**, 038102 (2008).
[37]M. Molaei and J. Sheng, "Succeed escape: Flow shear promotes tumbling of *Escherichia coli* near a solid surface," Sci. Rep. **6**, 35290 (2016).
[38]K. A. Fahrner, W. S. Ryu, and H. C. Berg, "Biomechanics: Bacterial flagellar switching under load," Nature **423**(6943), 938 (2003).
[39]S. Makarchuk, V. C. Braz, N. A. M. Araújo, L. Ciric, and G. Volpe, "Enhanced propagation of motile bacteria on surfaces due to forward scattering," Nature Communications **10**, 4110 (2019).
[40]Y. Park, Y. Kim, and S. Lim, "Flagellated bacteria swim in circles near a rigid wall," Phys. Rev. E **100**, 063112 (2019).
[41]J. Ainley, S. Durkin, R. Embid, R. Boindala, and R. Cortez, "The method of images for regularized Stokeslets," J. Comp. Phys. **227**, 4600–4616 (2008).
[42]R. Cortez and D. Varela, "A general system of images for regularized Stokeslets and other elements near a plane wall," J. Comp. Phys. **285**, 41–54 (2015).
[43]S. Lim, A. Ferent, X. S. Wang, and C. S. Peskin, "Dynamics of a closed rod with twist and bend in fluid," SIAM J. Sci. Comput. **31**, 273–302 (2008).
[44]S. Olson, S. Lim, and R. Cortez, "Modeling the dynamics of an elastic rod with intrinsic curvature and twist using a regularized Stokes formulation," J. Comput. Phys. **238**, 169–187 (2013).

[45]J. J. Higdon, "The hydrodynamics of flagellar propulsion: Helical waves," J. Fluid Mech. **94**, 331–351 (1979).
[46]E. Lauga, "Bacterial hydrodynamics," Annu. Rev. Fluid Mech. **48**, 105–130 (2016).
[47]N. C. Darnton and H. C. Berg, "Force-extension measurements on bacterial flagella: Triggering polymorphic transformations," Biophys. J. **92**, 2230–2236 (2007).
[48]H. C. Berg and R. A. Anderson, "Bacteria swim by rotating their flagellar filaments," Nature **245**, 380–382 (1973).
[49]M. T. Brown, B. C. Steel, C. Silvestrin, D. A. Wilkinson, N. J. Delalez, C. N. Lumb, B. Obara, J. P. Armitage, and R. M. Berry, "Flagellar hook flexibility is essential for bundle formation in swimming *Escherichia coli* cells," J. Bacteriol. **194**, 3495–3501 (2012).
[50]L. Turner, L. Ping, M. Neubauer, and H. C. Berg, "Visualizing flagella while tracking bacteria," Biophys J. **111**, 630–639 (2016).
[51]G. Junot *et al.*, "Run-to-tumble variability controls the surface residence times of *E. coli* bacteria," Phys. Rev. Lett. **128**, 248101 (2022).
[52]G. Sharma, S. Sharma, P. Sharma, D. Chandola, S. Dang, S. Gupta, and R. Gabrani, "*Escherichia coli* biofilm: Development and therapeutic strategies," J. Appl. Microbiol. **121**(2), 309–319 (2016).
[53]G. Li and J. X. Tang, "Accumulation of microswimmers near a surface mediated by collision and rotational Brownian motion," Phys. Rev. Lett. **103**, 078101 (2009).
[54]M. Hintsche *et al.*, "A polar bundle of flagella can drive bacterial swimming by pushing, pulling, or coiling around the cell body," Sci. Rep. **7**, 16771 (2017).
[55]M. J. Kuhn, F. K. Schmidt, B. Eckhardt, and K. M. Thormann, "Bacteria exploit a polymorphic instability of the flagellar filament to escape from traps," Proc. Natl. Acad. Sci. U. S. A. **114**, 6340–6345 (2017).
[56]Y. Kinosita, Y. Kikuchi, N. Mikami, D. Nakane, and T. Nishizaka, "Unforeseen swimming and gliding mode of an insect gut symbiont, *Burkholderia* sp. RPE64, with wrapping of the flagella around its cell body," ISME J. **12**, 838–848 (2018).
[57]J. Park, Y. Kim, W. Lee, and S. Lim, "Modeling of lophotrichous bacteria reveals key factors for swimming reorientation," Sci. Rep. **12**, 6482 (2022).
[58]J. Hill, O. Kalkanci, J. L. McMurry, and H. Koser, "Hydrodynamic surface interactions enable *Escherichia coli* to seek efficient routes to swim upstream," Phys. Rev. Lett. **98**, 068101 (2007).
[59]T. Kaya and H. Koser, "Direct upstream motility in *Escherichia coli*," Biophys. J. **102**, 1514–1523 (2012).
[60]P. E. Arratia, "Life in complex fluids: Swimming in polymers," Phys. Rev. Fluids **7**, 110515 (2022).